Available online at www.sciencedirect.com
ScienceDirect
Acta Materialia 59 (2011) 4416–4424
Acta MATERIALIA
www.elsevier.com/locate/actamat

Size effects in Al nanopillars: Single crystalline vs. bicrystalline

Allison Kunz, Siddhartha Pathak, Julia R. Greer *

Division of Engineering and Applied Sciences, California Institute of Technology, 1200 East California Boulevard, MC 309-81, Pasadena, CA 91125-8100, USA

Received 31 January 2011; received in revised form 25 March 2011; accepted 25 March 2011
Available online 22 April 2011

Abstract

The mechanical behavior of bicrystalline aluminum nano-pillars under uniaxial compression reveals size effects, a stochastic stress–strain signature, and strain hardening. Pillar diameters range from 400 nm to 2 μm and contain a single, non-sigma high angle grain boundary oriented parallel to the pillar axes. Our results indicate that these bicrystalline pillars are characterized by intermittent strain bursts and exhibit an identical size effect to their single crystalline counterparts. Further, we find that the presence of this particular grain boundary generally decreases the degree of work hardening relative to the single crystalline samples. These findings, along with transmission electron microscopy analysis, show that nano-pillar plasticity in the presence of a grain boundary is also characterized by dislocation avalanches, likely resulting from dislocation nucleation-controlled mechanisms, and that at these small length scales this grain boundary may serve as a dislocation sink rather than a dislocation source.

Keywords: Compression test; Nanoindentation; Electron backscatter diffraction; Interfaces; Aluminum

1. Introduction

The development of uniaxial micro-mechanical testing has led to a renaissance of research in mechanical metallurgy. The original work by Uchic et al. [1] demonstrated that cylindrical Ni pillars with micron scale diameters, fabricated using the focused ion beam (FIB) technique, exhibited an entirely new behavioral regime: discrete strain "bursts", low hardening rates even for large strains, and a power law relationship between flow stress and pillar diameter [2]. A large number of subsequent nano- and micro-pillar studies revealed similar stress–strain curves and identical size effects for a number of fcc metals [3–8]. Remarkably, the power-law size effect proved to be consistent for all fcc metals, generally of the form $\sigma_f \propto D^n$, where D is the pillar diameter and n is of the order of -0.6. While the origins of this size effect are a matter of intense debate, it is generally agreed that the higher stresses attained during mechanical deformation of small scale crystals are a result of nucleation-governed plasticity. Mobile dislocations inside these pillars are attracted to the free surface in response to the image forces, and new dislocations have to be nucleated either in the bulk of the pillar or on its surface in order to accommodate further deformation. Deep in the sub-micron regime it has been shown that the strained fcc pillars experience "hardening by dislocation starvation", whereby mobile dislocations exit the pillar at the free surface at a faster rate than they multiply [3,9]. A convincing example of this concept is the "mechanical annealing" of nickel in an in situ transmission electron microscopy (TEM) compression study by Shan et al. [10].

Since 2005 nano-mechanical testing of pillars has quickly evolved and expanded. New fabrication methods and custom built in situ mechanical equipment allow uniaxial tension experiments in addition to compression tests [11–16]. As first shown by Kiener et al., samples with heads suitable for tension testing and corresponding nano-indenter "grippers" can be made using FIB technology [17,18]. Electroplating methods have also produced

* Corresponding author.
E-mail address: jrgreer@caltech.edu (J.R. Greer).

1359-6454/$36.00
doi:10.1016/j.actamat.2011.03.065

Cu pillars for both uniaxial tension and compression testing, with the additional capability of creating pillars with diameters below 100 nm [19,20]. Beyond fcc, the effect of size on strength for a variety of crystal structures has been investigated, including bcc [21–29] and hcp [30–32]. Computational techniques like molecular dynamics (MD) [33–35] and dislocation dynamics (DD) [36,37] have also been widely utilized to shed light on the underlying defect mechanisms leading to this size-dependent strengthening. For example, MD simulations of fcc and bcc nano-pillars by Weinberger et al. demonstrate dislocation starvation in the former and dislocation multiplication in the latter [38,39]. DD simulations generally reveal the operation of truncated Frank–Read sources, or so-called "single-arm sources" [40]. The experimental and computational findings on mostly micron sized fcc pillars in compression up to 2008 can be found in a thorough review by Uchic et al. [41], while a recent review by Greer and de Hosson [42] offers a discussion on subsequent size effects studies spanning other materials and sub-micron sizes.

While so far most groups have focused on studying size effects in monolith systems such as single crystals, several researchers have looked at more complex microstructures, such as nano-crystalline [43], nano-twinned [44,45], nano-laminate [46,47], and alloyed materials [48,49], to name a few. For example, Jang et al. found a "smaller is weaker" phenomenon in nanocrystalline Ni–W pillars with an average grain size of 60 nm [50], while Mara et al. found that the presence of closely spaced Cu–Nb nano-laminates overrides the size effect, with the strength being a function of the laminate spacing rather than the sample dimensions [46]. Several computational studies investigating deformation of small scale interface-containing metallic systems have also been published and were summarized in a recent review by Zhu and Li [51]. In many cases the presence of internal boundaries has an effect on the size-dependent strength. These results are especially relevant for industrial applications, since most engineering materials are usually polycrystalline or multiphase rather than perfect single crystals. However, most reported literature on the mechanical properties of such materials reveals the aggregate effects of many interfaces rather than the role of individual interfaces. Therefore, the fundamental questions about the effects of individual interfaces, for example the relative influences of different types of interfaces (homogeneous vs. heterogeneous, coherent vs. incoherent, internal vs. free surface, etc.) on dislocation motion and overall sample plasticity, remain elusive.

This work compares the uniaxial compression results of single crystalline and bicrystalline aluminum pillars with diameters between ~400 nm and 2 μm. The bicrystalline pillars contain a single grain boundary vertically oriented along the pillar axis. We report the emergence of an identical size effect regardless of the presence of a boundary, and discuss their deformation in the framework of nucleation-controlled plasticity.

2. Experiments

Commercially available high purity aluminum (5 N purity, ESPI Metals) was annealed under vacuum at 350 °C overnight and then electropolished by Able Electropolishing Co. Grain orientation maps were obtained by automatic indexing of electron backscatter diffraction (EBSD) patterns using a Zeiss1550 VP field emission scanning electron microscope equipped with an EBSD system from Oxford Instruments, as shown in Fig. 1a. Once a high angle grain boundary of suitable length had been located, nanopillar samples containing this boundary close to the center of each sample were fabricated using a FEI Nova 200 scanning electron microscope with a focused ion beam (FIB) according to the procedure outlined in Greer et al. [2]. All nano-pillars had height to width ratios between 3:1 and 4:1, as well as less than 2° of vertical taper, with diameters ranging from roughly 400 to 2000 nm. Bicrystalline pillars contained the grain boundary oriented lengthwise, along the pillar or loading axis. A scanning electron microscopy (SEM) image of a representative bicrystalline pillar with overlaid EBSD pattern is shown in Fig. 1b. Single crystalline nanopillars were made using the same methodology in the two grains adjacent to the high angle boundary.

Uniaxial compression tests were conducted using a Nanoindenter G200 (Agilent Technologies). Using the dynamic contact module (DCM) with a 7 μm diameter flat punch we were able to simultaneously measure load, displacement, and harmonic contact stiffness during the tests. The tests were performed under displacement rate control via a feedback loop to attain a constant 0.001 s^{-1} strain rate until 15% strain. True stress and true strain, including the Sneddon correction, were calculated using the method also outlined in Greer et al. [2]. For each test the harmonic contact stiffness data were compared with the theoretical stiffness to ensure accurate effective pillar dimensions. SEM images of a bicrystalline pillar before and after uniaxial compression are given in Fig. 1c and d, respectively.

In order to determine the oxygen content in the aluminum sample and, hence, the extent of the native oxide layer on the sample surface, quantitative energy-dispersive X-ray spectroscopy (EDS) measurements (Oxford Instruments INCA 4.08) were performed using the same electron microscope as for the EBSD study. The results for the aluminum sample were compared with those for gold, tungsten, niobium, titanium and Fe–3% Si steel, all analyzed during the same session at 5 keV and a working distance of 10 mm. The process was repeated on a second day for consistency. The wt.% (wt.% = apparent concentration/intensity correction) of the element was calculated from the EDS spectrum after correcting for inter-element effects using the XPP matrix correction scheme built-in in the INCA software. The at.% (at.% = wt.%/atomic weight) was calculated from the measured wt.% values for each element, with the sum of atomic weights of all elements in the sample being normalized to 100%.

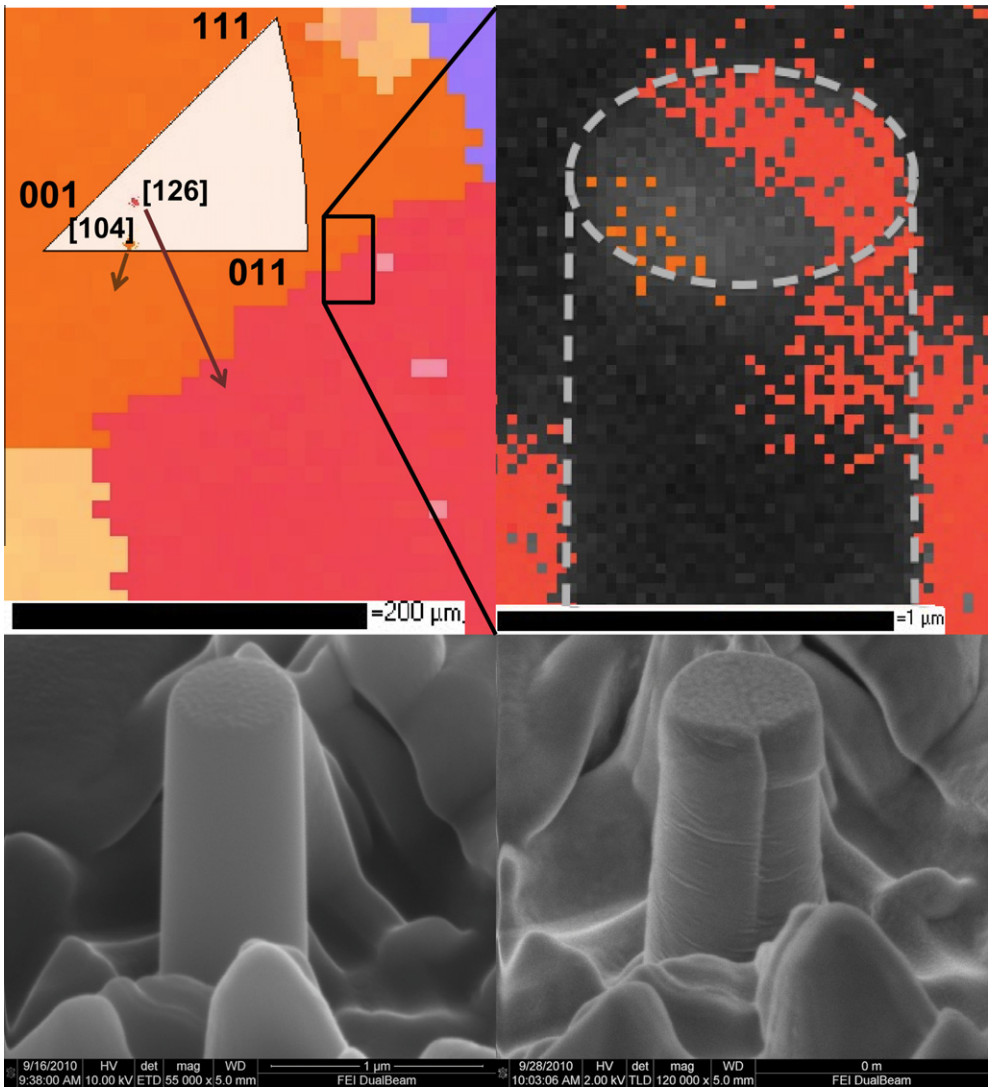

Fig. 1. (a) Crystallographic orientation map of a polycrystalline aluminum sample. (Inset) The inverse pole figure. (b) EBSD image of a typical grain boundary in a pillar. SEM images of the pillars (c) before and (d) after compression to 15% strain.

Transmission electron microscopy (TEM) of a representative post-compression bicrystalline nano-pillar was conducted using an FEI Tecnai F-20 microscope. To prepare the TEM sample a micron thick protective coating of tungsten was deposited on the nanopillar using the Nova 200, and a segment containing the coated pillar on a coupon of the underlying parent material was milled out. A micromanipulator (Omniprobe) was used to lift out the segment, which was then glued to a copper TEM lamella with additional tungsten deposition. FIB cleaning of cross-sections at very low currents of 10 pA and 30 kV was used to thin the pillar-containing segment of aluminum down to less than 100 nm thick.

3. Results

Representative compressive stress–strain curves for single crystalline nano-pillars from each grain and for bicrystalline aluminum nano-pillars are presented in Fig. 2. All of the curves exhibit the discrete stochastic bursts that are characteristic of small scale fcc deformation. The orientation information provided by EBSD was used to calculate the anisotropic Young's modulus $E_{[hkl]}$ and maximum Schmid factors for each orientation. To calculate the modulus of the bicrystalline pillars we assumed an isostrain model with equal volume fractions for both grains. Since aluminum is fairly isotropic (the theoretical values for $E_{[126]}$ and $E_{[104]}$ differ by only 2.7%), any uncertainty about the exact volume fraction of each grain did not have a significant effect on the bicrystalline data analysis. The average slopes of the unloading curves matched their respective theoretical Young's moduli $E_{[hkl]}$ to within 5%. Table 1 provides the Euler angles, Young's moduli, both calculated and measured, and the Schmid factors for the first available slip system for each type of pillar.

The flow stresses at 7.5% strain for single crystalline and bicrystalline samples, resolved by their respective Schmid factors, are plotted as a function of pillar diameter in

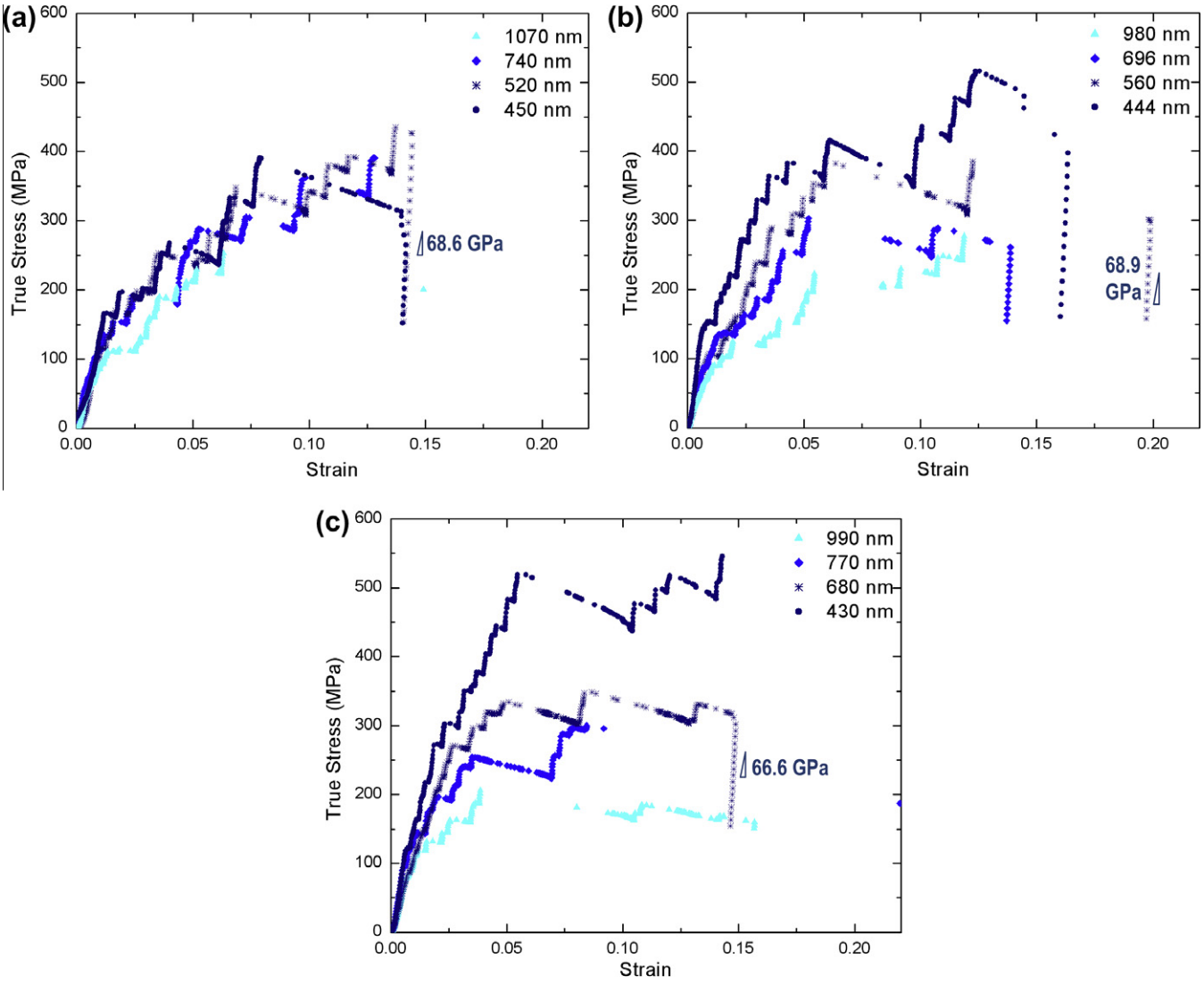

Fig. 2. Representative stress–strain curves for single crystalline pillars oriented with Z in the (a) [1 0 4] and (b) [1 2 6] directions, as well as (c) bicrystalline pillars created at the boundary between two grains.

Table 1
Summary of the crystallographic data and size effects.

Pillar type	Euler angle	$E_{[hkl]}$(GPa)		Schmid factor	Slip systems	Power law coefficient n	R^2
		Calculated	Measured				
Single-crystalline						−0.625	0.656
[126]-oriented	19.2, 18.4, 28.1	65.72	68.63	0.4879	(1 −1 −1) [−1 0 −1]	−0.629	0.788
[104]-oriented	269.1, 15.5, 85.5	67.50	68.87	0.4803	(1 1 1) [0 1 −1], (−1 1 −1) [0 1 1]	−0.578	0.689
Bicrystalline		66.61	64.85	0.4841		−0.590	0.715

Fig. 3a and b. Note that the highly stochastic nature of the nano-pillar deformation, combined with possible uncertainty at initial loading between the pillar and the punch, make an unambiguous determination of the yield (elastic to plastic transition) very difficult. Calculating the flow stress at 7.5% strain, on the other hand, removes this ambiguity, since this particular strain level is after full contact has been established, but before the stochastic nature of the bursts obscures precise determination of flow stress.

The data for the single crystalline pillars (Fig. 3a) reproduces the expected power law relationship between the resolved shear flow stress and pillar diameter with a slope of −0.625, nearly identical to that observed for most non-pristine fcc metals [41]. Fig. 3b compares the single

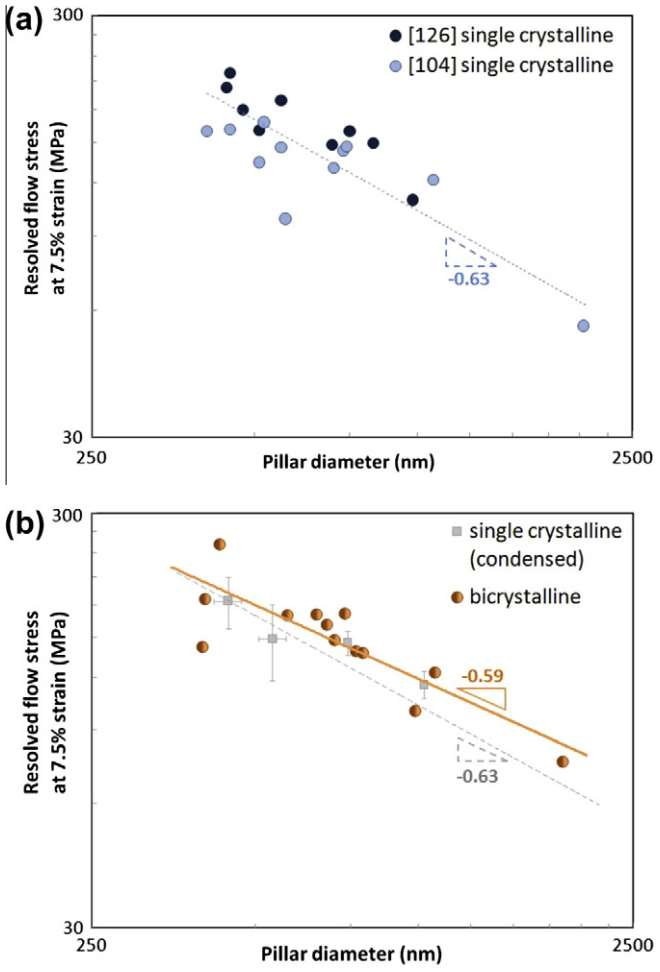

Fig. 3. Size effect plots showing the power law relationship between pillar diameter and flow stress for (a) single crystalline and (b) single crystalline (condensed) vs. bicrystalline pillars. The error bars reflect the standard deviation.

crystalline data shown in Fig. 3a, condensed into fewer points with error bars reflecting the standard deviations for clarity, with the bicrystalline results. Interestingly, we find that the size effect exhibited by the bicrystalline samples is nearly equivalent to the single crystalline ones: the pillars containing grain boundaries give a slope of −0.590, which is only a 5.6% difference from the single crystalline case. Another interesting observation that can be made based on this data is that the bicrystalline pillars and [104]-oriented single crystalline pillars show a significantly larger spread in flow stresses after 5% strain than the tightly distributed [126]-oriented single crystalline pillars. We ascribe this to the fact that the [104] direction is favorably oriented for bi-slip, with two slip systems sharing the highest Schmid factor values, while [126] is oriented for single slip only. Table 1 shows a summary of the primary slip systems for each orientation, as well as their Schmid factors and elastic moduli. The power law coefficients n and their R^2 values are also included in Table 1.

We also investigate the amount of flow stress increase with increasing strain for each pillar type. Since the deformation of these nano-structures is characterized by intermittent strain bursts, the conventional definition of strain hardening is ill suited here. Instead, we define our hardening figure of merit as the angle calculated from the slope of the region between full flat punch–pillar contact and the beginning of unloading on the stress–strain curves. This slope is normalized to the flow stress at 7.5% strain in order to deconvolute any pillar size effect from the hardening data. We note, however, that these behavioral regimes are evident even without normalization of the hardening slope with the flow stress. The point of full contact was determined by the strain at which the measured harmonic contact stiffness matched the theoretical stiffness calculated from the effective pillar dimensions. A schematic outlining this procedure on a representative stress–strain curve, as well as the corresponding stiffness plot, are shown in Fig. 4. Due to the uncertainty in the measurements immediately following a strain burst, when the indenter lags behind the pillar deformation, only peak values in the loading direction of each burst were used to represent the applied stress. These hardening angles normalized to the 7.5% flow stresses are plotted as a function of pillar diameter in Fig. 5. Only samples for which the hardening angles could be reliably calculated, i.e. with enough burst peaks to obtain a reliable average slope, are included in the figure. Note also that the constraints imposed by the experimental set-up are known to affect pillar hardening, as studied by Dehm et al. [52], and thus only tests conducted using the same set-up can be directly compared with each other. As can be seen from Fig. 5, the pillars containing grain boundaries exhibit lower average angles compared with their single crystalline counterparts, forming two adjacent behavioral regimes.

4. Discussion

Although the size effect here appears to remain unchanged despite the presence of this particular grain boundary, the stress–strain curves of single crystalline vs. bicrystalline samples exhibit distinct characteristics. First, we compare the data for single crystalline pillars fabricated from the two adjacent grains with each other. Figs. 2a and b and 3a show that the [104]-oriented single crystalline pillars exhibit a shorter average burst size and less pronounced size effect. In order to understand the mechanisms behind these different characteristics we return to the EBSD analysis of the grain orientations. The inverse pole figure in Fig. 1a indicates that the [126] orientation corresponds to single slip, while the [104] orientation is likely to experience double slip. Previous work by Ng and Ngan [53] has shown the collapse of Schmid's law during uniaxial compression of aluminum sub-micron pillars: this research found that as the volume of the pillar decreases the probability that a dislocation exists in the theoretically favored slip orientation (maximum Schmid factor) also decreases. Thus, in smaller pillars the dislocations residing in the slip planes less favored for slip

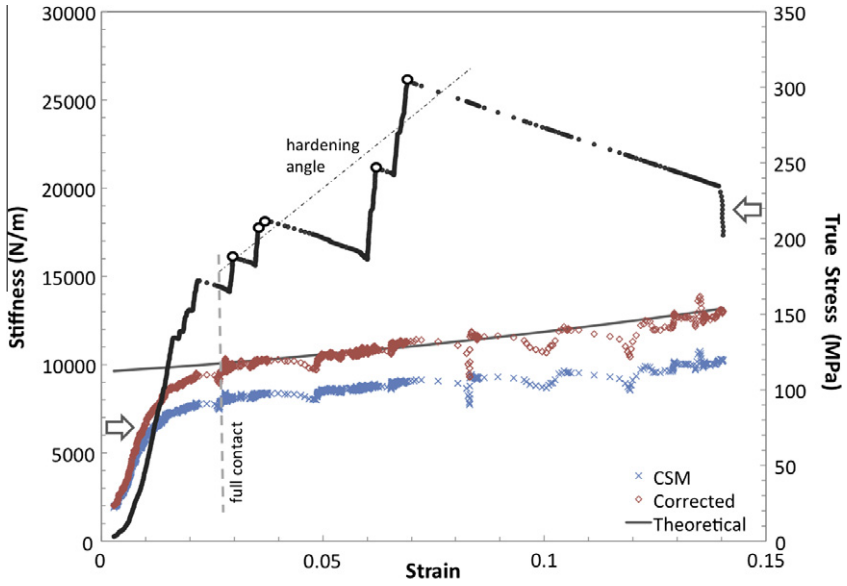

Fig. 4. Compression data analysis. Both the instrument contact stiffness measurements (CSM) and data adjusted with the Sneddon correction from Greer et al. [2], are plotted, along with the theoretical stiffness. The stress–strain curve from the same pillar is also given, with peak values following full contact in bold and their hardening angle indicated by the black dashed line.

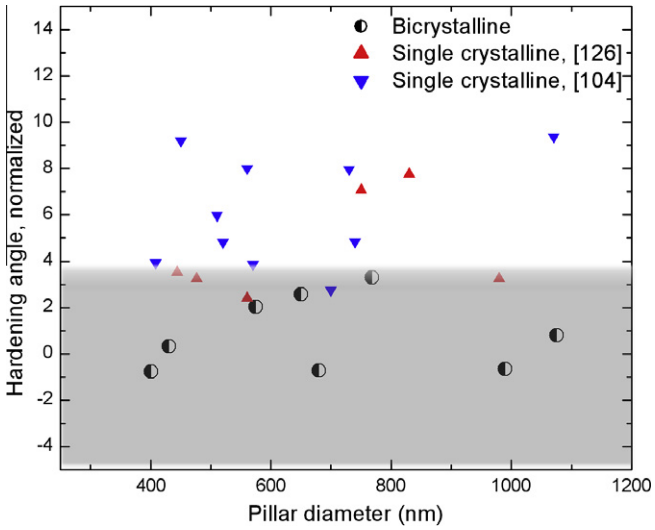

Fig. 5. Plot of hardening angle vs. pillar diameter for the three sets of pillars. The shaded area emphasizes the lower average hardening angle for bicrystalline pillars relative to single crystalline ones.

may possibly be the ones available for slip, thereby requiring higher resolved shear stresses for their activation. Multiple slip provides a greater number of equivalent slip systems, which increases hardening through shortening the dislocation mean free path, manifesting itself as a shorter average burst size. Deforming pillars with an imperfect double slip orientation, meaning that some nominally double slip oriented pillars deform via symmetrical slip, others via single slip, would lead to a greater variability in yield stresses and hardening behavior. All of these characteristics are consistent with our data for [104]-oriented samples. On the other hand, the [126]-oriented samples show consistent hardening and a well-defined size effect. The behavior of the bicrystalline samples resembles more closely that of the [126] pillars oriented for single slip than the [104]-oriented samples oriented for double slip. This similarity is likely due to the slightly higher Schmid factor for the [126] crystal orientation, which would therefore be more likely to yield first. However, there is much less hardening in the bicrystalline samples compared with single crystalline ones in both orientations.

The relatively large average burst sizes (Fig. 2c) and the much lower hardening angles (Fig. 5) in the bicrystalline samples may imply one of three scenarios. In the first two cases either the dislocations travel unimpeded over appreciable distances causing little or no dislocation storage, or the dislocations pile up at obstacles (such as a boundary) and are collectively emitted in relatively large bursts. These two observations might suggest that this particular grain boundary serves as a sink rather than a source of dislocations under applied uniaxial compressive loads. These results agree well with the classical work of Dollar and Gleiter [54], who showed that random high angle boundaries in an irradiated Au foil act as perfect dislocation sinks. Recent nanoindentation studies by Pathak et al. [55] and EBSD measurements by Sun et al. [56] have also demonstrated the ability of high angle grain boundaries to act as efficient dislocation sinks as a function of applied strain.

The third possibility is that the grain boundary itself undergoes some kind of localized breakdown and compatibility loss. Such a scenario was discussed in the work of Ng and Ngan [57], in which the authors noted intense shear of the grain boundary during uniaxial compression of ~6 μm diameter bicrystalline aluminum micro-pillars. As discussed later, TEM micrographs of our bicrystalline pillars

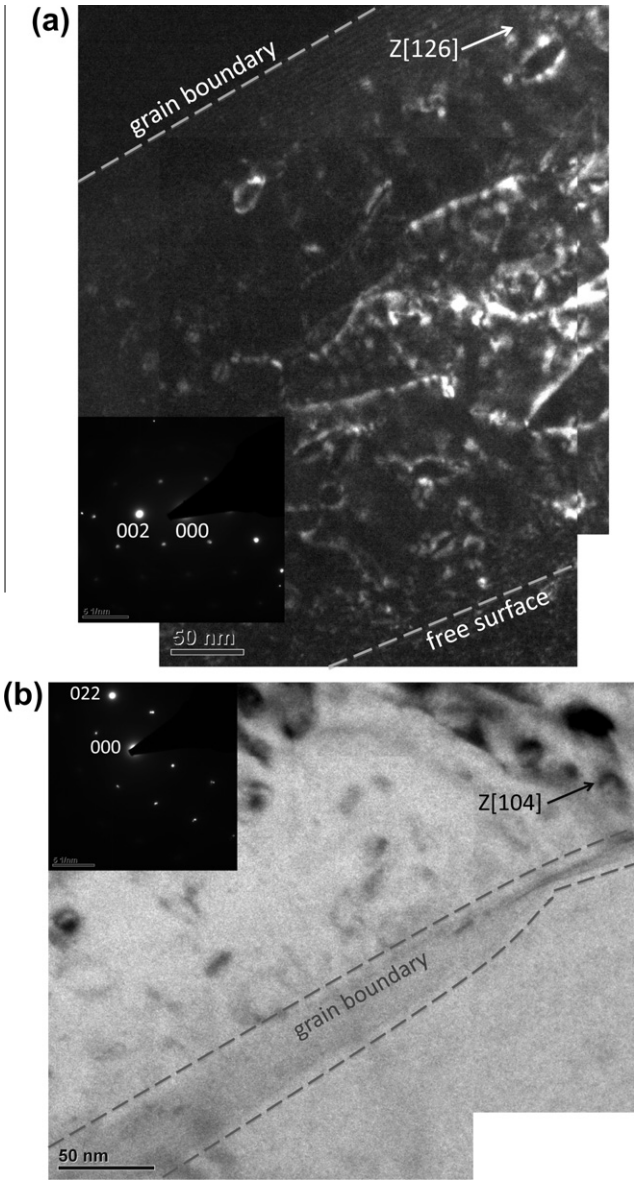

Fig. 6. (a) Dark field TEM image of the [126]-oriented half and (b) bright field TEM image of the [104]-oriented half of the same bicrystalline pillar after uniaxial compression to 15% strain. FIB damage, in the form of dislocation loops, is evident in both sets of images.

(Fig. 6) corroborate this possibility, as it is evident that the boundary itself was altered in the course of compression. Thus, when exposed to sufficiently high stresses, such as those experienced by our nano-pillars, such grain boundary relief (or breakdown) mechanisms could also potentially trigger the significantly larger bursts in our bicrystalline pillars shown in Fig. 2c. Note that such large bursts were not observed in the work of Ng and Ngan [57], probably because the micron sized pillars used in their study experienced roughly an order of magnitude lower stresses than our nanoscale bicrystalline pillars. The exact nature and possibility of the grain boundary breakdown mechanism still remains to be explored in detail, and efforts addressing this aspect are currently underway.

Interestingly, continuum-based crystalline plasticity simulations accounting for the discrete behavior of the dislocation bursts have also noted a larger first burst during compression of bicrystalline, as well as single crystalline, Al pillars [58]. This is explained by simultaneous competition by multiple slip systems for accommodation of the shear stress prior to the first burst. Additionally, one localized slip will only be accommodated if the neighboring region, still free of defects, can also accommodate slip propagation. The presence of a boundary could potentially accentuate this first burst, and efforts are currently underway to conduct a statistical analysis comparing such burst distributions between single and bicrystalline samples, which will be disseminated in a separate manuscript.

Of note is the exact opposite effect seen by Ng and Ngan [57], whose bicrystalline aluminum micro-pillars displayed larger hardening angles compared with their single crystal counterparts by a factor of nearly 2.5. However, the grain boundaries in their study had completely different grain boundary characteristics in terms of crystallographic orientations and boundary misorientations. Also, their boundaries were not positioned lengthwise down the pillar, parallel to the loading axis, but instead at a large angle to the loading axis, with one end exiting the pillar through the cylinder wall. These differences indicate the importance of understanding the grain boundary characteristics and orientation when analyzing such cases. Also, the size of their samples was nearly an order of magnitude larger than ours, allowing enough space to form an intertwined dislocation sub-structure.

To further understand microstructural evolution in the bicrystalline pillars we performed TEM analyses on a representative post-mortem sample, shown in Fig. 6, which reveals no evidence of dislocations piling up at the grain boundary. Fig. 6a provides dark field images with

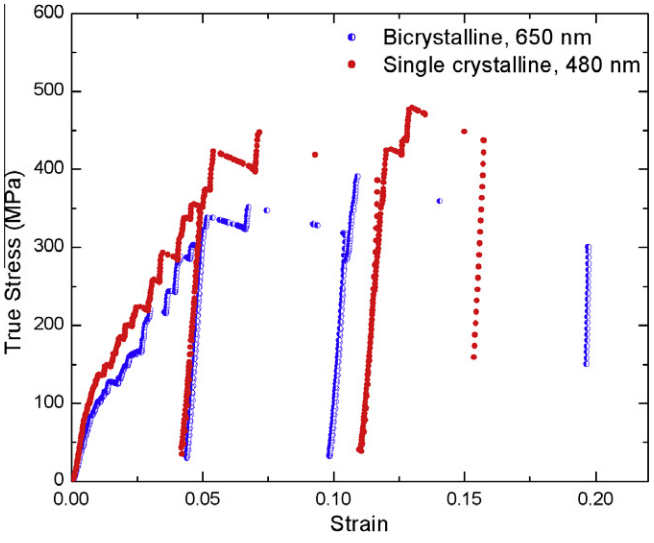

Fig. 7. Stress–strain curves from representative single and bicrystalline pillars subjected to cyclic uniaxial compression testing, showing no Bauschinger effect.

Table 2
Quantitative EDS analysis results.

	Gold	Aluminum	Tungsten	Niobium	Titanium	Fe–3% Si steel
wt.%	O K: 0 Au M: 100	O K: 2.04 ± 0.34 Al K: 97.96 ± 0.34	O K: 1.38 ± 0.26 W M: 98.62 ± 0.26	O K: 4.97 ± 0.43 Nb L: 95.03 ± 0.43	O K: 0.83 ± 0.37 Ti K: 99.17 ± 0.37	O K: 2.07 ± 0.29 Si K: 2.7 ± 0.29 Fe L: 95.46 ± 0.41
at.%	O K: 0 Au M: 100	O K: 3.42 Al K: 96.58	O K: 13.93 W M: 86.07	O K: 23.17 Nb L: 76.83	O K: 2.45 Ti K: 97.55	O K: 6.69 Si K: 4.46 Fe L: 88.85

$g = 002$ near the [1 1 0] zone axis for the [126]-oriented half of the pillar; the sample tilt resulted in a brightness gradient across the images. Dislocations are clearly visible, with the smaller, looped dislocations probably being the result of FIB damage and the longer dislocation segments probably associated with pillar deformation. The FIB damage appears to have an even distribution across the entire surface, a common effect observed by several groups [59–61], while the dislocations associated with deformation appear to be concentrated in the center of the half-pillar, as opposed to near the free surface or the grain boundary. Fig. 6b is a representative higher magnification bright field image with $g = 022$ near the [1 0 0] zone axis for the [104]-oriented half of the same pillar, where again we see evidence of FIB damage, but not of dislocations associated with deformation. It is especially compelling that the regions next to the grain boundary in both grains are relatively defect free. This lack of evidence of dislocation pile-ups at the grain boundary and the presence of a so-called "denuded zone" [54], a region free of defect agglomerates near an interface, is consistent with our hypothesis that this boundary serves as a dislocation sink. A distinct rotation of the grain boundary is also observed in the bright field image (Fig. 6b), suggesting that the grain boundary itself is deforming, although the mechanism remains to be further investigated.

The presence of a native oxide film on the sample surfaces may be a concern in our experiments, as it may trap the dislocations inside the pillar, generate dislocation pile-ups against the pillar–oxide interface, and require higher deformation stresses. Previous work on single crystalline aluminum micro-pillars by Ng and Ngan [62] illustrated that a nanocrystalline tungsten coating both increased the yield stresses and suppressed the discrete nature of the stress–strain curves. Simulations by Deshpande et al. [63] and thin film experiments by Nicola et al. [64] also showed that surface passivation results in significantly more pronounced work hardening and a clear Bauschinger effect. Aluminum is known to generate a 5–10 nm oxide layer on its surface, and in order to test its effect on our pillar compression experiments we ran intentional loading–unloading segments during the compression tests on both single and bicrystalline nano-pillar samples, the results of which are shown in Fig. 7. As seen from this plot, neither stress–strain curve indicates strong hardening or a Bauschinger effect, indicating that the native oxide layer does not serve as a passivation layer, and, therefore, probably does not play a significant role in plastic deformation at this length scale. Similarly, the EDS results shown in Table 2 indicate that the weight percentage of oxygen in aluminum (~2 wt.%) is comparable with that of W, Nb, Ti and Fe–3% Si steel, metals whose size effects have been reported by multiple groups [22,27,57]. Note that the EDS data is limited to only a weight estimation of the oxygen content; it does not provide any information on the mechanical strength of the oxide itself. Table 2 also indicates that, other than noble metals such as gold, all of the other metals tested have a layer of native oxide on their surface which has not been shown to affect their mechanical behavior at submicron length scales [21,22]. The low oxygen weight percentages in Al, when combined with the lack of a Bauschinger effect shown in Fig. 7, may indicate that the surface aluminum oxide is unlikely to contribute greatly to the mechanical strength of the aluminum nano-pillars in compression experiments.

5. Conclusions

We have examined the effect of a vertical, non-sigma, high angle grain boundary on the mechanical properties and deformation behavior of sub-micron Al pillars subjected to uniaxial compression. We observe similar stress–strain signatures, containing numerous discrete displacement bursts, as well as an identical power law "smaller is stronger" size effect in these bicrystalline samples as compared with their single crystalline counterparts. We also observe lower hardening angles and larger burst extents in the bicrystalline pillars, implying little or no dislocation storage and suggesting that this grain boundary may act as a dislocation sink. TEM analysis confirms this hypothesis, as the near boundary regions appear to be defect free, with no evidence of dislocation pile-ups. Since similar work on larger sized bicrystalline aluminum pillars with a different type of grain boundary exhibited the opposite effect: smaller burst sizes and increased hardening, this study reveals that the character of the boundary and sample size appear to play a significant role in the deformation behavior. Efforts are currently underway at comparing the effects of grain boundaries with very different characters on deformation behavior.

Acknowledgements

S.P. gratefully acknowledges the support from the W.M. Keck Institute for Space Studies Postdoctoral Fellowship

program. J.R.G. gratefully acknowledges financial support from an NSF Career award (DMR-0748267). The authors also thank Andrew T. Jennings and Carol Garland for TEM assistance and A. Fernandez, A. Jerusalem, and C. Weinberger for useful discussions.

References

[1] Uchic MD, Dimiduk DM, Florando JN, Nix WD. Science 2004;305:986.
[2] Greer JR, Oliver WC, Nix WD. Acta Mater 2005;53:1821.
[3] Greer JR, Nix WD. Phys Rev B 2006;73:245410.
[4] Volkert CA, Lilleodden ET. Phil Mag 2006;86:5567.
[5] Ng KS, Ngan AHW. Acta Mater 2008;56:1712.
[6] Dimiduk DM, Uchic MD, Parthasarathy TA. Acta Mater 2005;53:4065.
[7] Budiman A, Han S, Greer JR, Tamura N, Patel J, Nix WD. Acta Mater 2007;56:602.
[8] Kiener D, Motz C, Schoberl T, Jenko M, Dehm G. Adv Eng Mater 2006;8:1119.
[9] Zheng H, Cao A, Weinberger CR, Huang JY, Du K, Wang J. Nat Commun 2010;1:144.
[10] Shan ZW, Mishra R, Syed SA, Warren OL, Minor AM. Nat Mater 2008:7.
[11] Greer JR, Kim J-Y, Burek MJ. J Mater 2009;61:19.
[12] Kiener D, Grosinger W, Dehm G. Scripta Mater 2009;60:148.
[13] Dehm G. Prog Mater Sci 2009;54:664.
[14] Legros M, Gianola DS, Motz C. MRS Bull 2010:35.
[15] Richter G, Hillerich K, Gianola DS, Monig R, Kraft O, Volkert CA. Nano Lett 2009;9:3048.
[16] Zhang D, Breguet J-M, Clavel R, Phillippe L, Utke I, Michler J. Nanotechnology 2009;20:365706.
[17] Kiener D, Grosinger W, Dehm G, Pippan R. Acta Mater 2008;56:580.
[18] Kim J-Y, Greer JR. Acta Mater 2009:57.
[19] Jennings AT, Greer JR. Philos Mag A 2010;DOI:10.
[20] Jennings AT, Burek MJ, Greer JR. Phys Rev Lett 2010:104.
[21] Kim J-Y, Jang D, Greer JR. Scripta Mater 2009;61:300.
[22] Kim J-Y, Jang D, Greer JR. Acta Mater 2010;58:2355.
[23] Han SM, Bozorg-Grayeli T, Groves JR, Nix WD. Scripta Mater 2010;63:1153.
[24] Bei H, Shim S, George EP, Miller MK, Herbert EG, Pharr GM. Scripta Mater 2007;57:397.
[25] Bei H, Shim S, Pharr GM, George EP. Acta Mater 2008;56:4762.
[26] Schneider AS, Kaufmann D, Clark BG, Frick CP, Gruber PA, Monig R, et al. Phys Rev Lett 2009:103.
[27] Schneider AS, Clark BG, Frick CP, Gruber PA, Arzt E. Mater Sci Eng A 2009;508:241.
[28] Zaiser M, Schwerdtfeger J, Schneider AS, Frick CP, Clark BG, Gruber PA, et al. Phil Mag 2008;88:3861.
[29] Lowry MB, Kiener D, LeBlanc MM, Chisholm C, Florando JN, Morris JWJ, et al. Acta Mater 2010;58:5160.
[30] Lilleodden E. Scripta Mater 2010;62:532.
[31] Byer CM, Li B, Cao B, Ramesh KT. Scripta Mater 2010;62:536.
[32] Yu Q, Shan Z-W, Li J, Huang X, Xiao L, Sun J, et al. Nature 2010;463:335.
[33] Cao A, Wei Y, Ma E. Phys Rev B 2008;77:195429.
[34] Deng C, Sansoz F. Acta Mater 2009;57:6090.
[35] Jin Z-H, Gumbsch P, Albe K, Ma E, Lu K, Gleiter H, et al. Acta Mater 2008;56:1126.
[36] Senger J, Weygand D, Gumbsch P, Kraft O. Scripta Mater 2008;58:587.
[37] Weygand D, Poignant M, Gumbsch P, Kraft O. Mater Sci Eng A 2008;483–484:188.
[38] Weinberger C, Cai W. Proc Nat Acad Sci USA 2008;105:14304.
[39] Greer JR, Weinberger C, Cai W. Mater Sci Eng A 2008;493:21.
[40] Lee S, Nix W. Mater Sci Eng A 2010;527:1903.
[41] Uchic MD, Shade PA, Dimiduk DM. Annu Rev Mater Res 2009:39.
[42] Greer JR, de Hosson JTM. Prog Mater Sci 2011. doi:10.1016/j.pmatsci.2011.01.005.
[43] Rinaldi A, Peralta P, Friesen C, Sieradzki K. Acta Mater 2008;56:511.
[44] Konstantin AA, Sansoz F. Nano Lett 2007;7:2056.
[45] Deng C, Sansoz F. Appl Phys Lett 2009;95:091914.
[46] Mara NA, Bhattacharyya D, Dickerson P, Hoagland RG, Misra A. Appl Phys Lett 2008;92:231901.
[47] Mara NA, Bhattacharyya D, Hirth JP, Dickerson P, Misra A. Appl Phys Lett 2010:97.
[48] San Juan JM, Nó ML, Schuh CA. Adv Mater 2008;20:272.
[49] Clark BG, Gianola DS, Kraft O, Frick CP. Adv Eng Mater 2010;12:808.
[50] Jang D, Greer JR. Scripta Mater 2011;64:77.
[51] Zhu T, Li J. Prog Mater Sci 2010;55:710.
[52] Kiener D, Motz C, Dehm G. Mater Sci Eng A 2009;505:79.
[53] Ng KS, Ngan AHW. Scripta Mater 2008;59:796.
[54] Dollar M, Gleiter H. Scr Metall 1985;19:481.
[55] Pathak S, Michler J, Wasmer K, Kalidindi S. Submitted for publication. 2011.
[56] Sun S, Adams BL, Shet C, Saigal S, King W. Scripta Mater 1998;39:501.
[57] Ng KS, Ngan AHW. Phil Mag 2009;89:3013.
[58] Jerusalem A. Private communications.
[59] Kiener D, Motz C, Rester M, Jenko M, Dehm G. Mater Sci Eng A 2006;459:262.
[60] Shim S, Bei H, Miller MK, Pharr GM, George EP. Acta Mater 2009;57:503.
[61] Kiener D, Motz C, Dehm G, Pippan R. Int J Mater Res 2009;100:1074.
[62] Ng KS, Ngan AHW. Acta Mater 2009;57:4902.
[63] Deshpande VS, Needleman A, Van der Giessen E. J Mech Phys Solids 2005;53:2661.
[64] Nicola L, Xiang Y, Vlassak JJ, Van der Giessen E, Needleman A. J Mech Phys Solids 2006:54 2089.